Extreme flow simulations reveal skeletal adaptations of deep-sea sponges

Giacomo Falcucci[1,2], Giorgio Amati[3], Pierluigi Fanelli[4], Vesselin K. Krastev[1], Giovanni Polverino[5], Maurizio Porfiri[6,8] & Sauro Succi[7,2,8]

[1]*Department of Enterprise Engineering "Mario Lucertini" - University of Rome "Tor Vergata"; Via del Politecnico 1, 00133 - Rome - Italy;*

[2]*Department of Physics - Harvard University; 17 Oxford St., 02138 Cambridge (MA) - USA;*

[3]*SCAI - SuperComputing Applications and Innovation Department, CINECA; Via dei Tizii, 6 - 00185 Rome - Italy;*

[4]*DEIM - School of Engineering - University of Tuscia; Largo dell'Università, 01100 Viterbo - Italy;*

[5]*Centre for Evolutionary Biology, School of Biological Sciences - University of Western Australia; 35 Stirling Highway, 6009 Perth - Australia;*

[6]*Department of Biomedical Engineering, Center for Urban Science and Progress, and Department of Mechanical and Aerospace Engineering - New York University Tandon School of Engineering; 370 Jay Street, 11201 Brooklyn (NY) - USA;*

[7]*Italian Institute of Technology; P.le Aldo Moro 1, 00185 Rome - Italy*

[8]*These authors contributed equally: Maurizio Porfiri, Sauro Succi.*

Since its discovery [1, 2], the deep-sea glass sponge *Euplectella aspergillum* has attracted the interest of scientists worldwide for remarkable mechanical properties and tantalising beauty.

A skeletal system composed of amorphous hydrated silica and arranged in a highly regular and hierarchical cylindrical lattice begets exceptional flexibility and resilience to damage [3–6]. Structural analyses dominate the literature, but hydrodynamic fields which surround and penetrate the sponge remain largely unexplored to date. A particularly outstanding question is whether, besides improving its mechanical properties, the skeletal motifs of *E. aspergillum* underlie the optimisation of the flow physics within and beyond its body cavity. This is precisely the question addressed in the present work. To this purpose, we resort to extreme flow simulations based on the Lattice Boltzmann method [7], featuring about one hundred billion grid points and spanning four spatial decades. These *in-silico* experiments reproduce the hydrodynamic conditions on the deep-sea floor where *E. aspergillum* lives [8–10]. Our results indicate that the skeletal motifs reduce the overall hydrodynamic stress and support coherent internal recirculation patterns at low flow velocity. These patterns are arguably beneficial to the organism for selective filter feeding and sexual reproduction [13, 14]. The present study reveals mechanisms of extraordinary adaptation to live in the abyssal, paving the way to a new class of numerical investigations at the intersection between fluid mechanics, organism biology, and functional ecology.

The progress in computational science has disclosed unique insights across virtually all fields of science, including the emerging frontier between physics and biology [15, 16]. The approach to exascale class computational facilities [17] promises unprecedented scientific analyses and predictions, allowing to explore questions beyond the reach of experimental investigations. As an example, the study of the profound connection between structure and function lies at the core of

modern biology, from cell cycles and metabolic analysis, all the way up to entire organs or the overall body of living creatures [18]. The availability of unprecedented computational power is enabling the study of realistically complex biological models, including deep-sea organisms that are often inaccessible to *in-vivo* experimentation. The main focus of the present work is the study of the fluid dynamic performance of deep-sea sponges in their actual living conditions, reproduced via *in-silico* experiments on "Marconi100", one of the most powerful computational facilities in the world [19].

Leveraging the versatility and resolution provided by extreme numerical simulations, we analysed different flow regimes corresponding to the actual living conditions of *E. aspergillum* shown in Fig. 1a. Through our simulations, performed via the Lattice Boltzmann method [7], we disentangled morphological characteristics in order to pin down the specific fluid dynamic role of each the skeletal features. The deep-sea sponge *E. aspergillum* (also known as Venus' flower basket) belongs to the oldest group of sponges (Hexactinellida) ever documented in the phylum Porifera [20]: it dwells at the bottom of the oceans, especially in the Pacific and around Antarctica, at depths of $100 - 1000$ m, with no ambient sunlight [21, 22]. The bottom of their body is anchored to the soft sediment of the sea floor and protrudes into the benthic boundary layer flow, thereby providing substrate for suspension feeders. Interestingly, a breeding pair of shrimps (Spongiicolidae family) that enter the cavity of the sponge through the small *fenestræ* on its surface will often be trapped in an eternally monogamous relationship as they grow in size — in Japanese Euplectella means "together for eternity" [23, 24]. *E. aspergillum* is characterised by exceptional structural properties which have sparked the attention of researchers since its discovery [1, 25,

26]. More specifically, the hierarchical arrangement of its skeletal system has proven to delay crack propagation and increase buckling strength [5, 27], thereby approaching an optimal material distribution [6]. Despite the vast literature on the mechanical properties of *E. aspergillum*'s skeletal system, to the best of our knowledge, the study of the surrounding and internal hydrodynamics has never been charted out to date.

We conducted extreme fluid dynamic simulations in order to assess the yet unknown hydrodynamic function of the different skeletal features of the sponge, under realistic living conditions, reproduced through different values of the water speed — hence different Reynolds numbers, $\mathrm{Re} = |\vec{u}|D/\nu$, where $\vec{u}$ is the water velocity, D the sponge diameter at its top section (~ 4 cm in our case [3]), and ν is the water kinematic viscosity ($\nu \sim 1.75 \times 10^{-6}$ m^2 [10], with potential variations of at most 15% due to modest changes in temperature and salinity in the abyssal [11, 12]). Based on the known, average distribution of water speed in proximity of the bottom of the ocean, which ranges between 0 and ~ 11 cm/s in the first 30 cm over the sea bed [9], we analysed the flow regimes corresponding to $\mathrm{Re} = 100,\ 500,\ 1000,\ 1500$, and 2000. These simulations provide unique insights into the ecological adaptions of *E. aspergillum* to live in extreme environments [28], revealing the flow-driven *raison d'être* for the sponge shape and its peculiar skeletal motifs.

For the complete model of *E. aspergillum* shown in Fig. 1b, simulations at statistical steady-state show a dramatic reduction of the flow speed inside the body cavity of the sponge, where low-speed vortical flow patterns are formed (see Fig. 1c). Surprisingly, such a quiescent region extends downstream the sponge in contrast with the wake behind solid obstacles [29]. Only several

diameters downstream, we observe the emergence of intermittent patterns [30, 31]. The complexity of the flow inside and outside the body cavity is evidenced by means of the contours of helicity ($\mathcal{H} = \vec{u}\cdot\vec{\omega}$, where $\vec{\omega} = \vec{\nabla}\times\vec{u}$ is the local flow vorticity, see Methods) and the streaklines coloured according to the flow speed: the presence of the quiescent region extending several diameters downstream the specimen is apparent from our *in-silico* experiments (see Extended Data Figs. 2 and 3 for more details).

To shed light into such a peculiar fluid dynamic behaviour and to clarify its dependence on *E. aspergillum*'s skeletal motifs, we conducted a series of *in-silico* morphological manipulations. We examined four simplified models of growing complexity, ranging from a solid cylinder to a hollow cylindrical lattice with helical ridges, which proxies the real morphology of the sponge without the anchoring to the seafloor. More specifically, we studied two solid models (S1, S2)— a plain cylinder (S1) and a cylinder with the same helical ridge patterns that decorate *E. aspergillum*'s skeletal system (S2)— and two porous models (P1, P2) with *fenestræ* on their surface — a hollow cylindrical lattice (P1) and a hollow cylindrical lattice with helical ridges (P2). All these geometries, reported in Fig. 1b, are subjected to periodic boundary conditions at the top and bottom. For each simplified model, we simulated the corresponding hydrodynamic field, and studied the downstream intermittency that arises for $\mathrm{Re} \geq 100$. We monitored the time evolution of the fluid velocity $\vec{u}(P,t)$ at a probe P located at a distance $2.5\ D$ downstream the model, $D/2$ from the symmetry axes along the flow direction, and $H/2$ from the bottom (H being the height of our computational domain). Figure 2a reports the time evolution of the three Cartesian components of the flow velocity $u_x(t), u_y(t), u_z(t)$ at the probe location P. The Figure refers to the final $\sim 1\%$

of the time evolution, well within the statistical steady-state of the given fluid regime. Results in Fig. 2a indicate that the two solid models are characterised by intense fluctuations of all three velocity components. By contrast, even at $\mathrm{Re} = 2000$, the porous models exhibit a dramatic suppression of such fluctuations. Moreover, we found that even at high Reynolds numbers ($\mathrm{Re} \geq 500$), the presence of the *fenestræ* in the porous models provides a suppression of the z-component of the fluid velocity, leading to a quasi-2D flow in the wake of the sponge (see Fig. 2a). The inclusion of local defects (simulating wounds and scars of the organism in the hollow cylindrical lattice with helical ridges, see Methods and Extended Data Fig. 4 for details) plays a secondary role on the flow velocity at P, whereby it contributes modest fluctuations of the order 10% of the peak-to-peak oscillations in the velocity components experienced by the solid models. The effect of Re on the uniformity of the flow field downstream the models under investigation is summarised in Fig. 2b, where the flow pattern exhibits a dramatic symmetry breaking above a critical value of Re. Symmetry breaking for the two solid models occurs at lower critical Re, indicating that the presence of the *fenestræ* provides a potent stabilising effect on the flow wake at high Re numbers, downstream the organism.

To further detail the role of the skeletal motifs of *E. aspergillum* on the downstream flow, we analysed the helicity $\mathcal{H}$ and enstrophy $|\vec{\omega}|^2$ fields (see Methods) of the hollow cylindrical lattice with helical ridges in comparison to those of the plain cylinder (P2 versus S1), as reported in Fig. 3. Figures 3a and b show a quiescent region downstream the porous model, which is absent for the solid one. The results are representative of the statistical steady-state reached at $\mathrm{Re} = 2000$, but the same findings are observed in all our simulations with $\mathrm{Re} \geq 500$ (see Extended Data Fig.

5). The helicity and enstrophy charts in Fig. 3b highlight that the quiescent region extends several diameters downstream the porous model. The extent of this region is robust with respect to the presence of local defects.

One of the implications of the presence of this nearly quiescent region downstream the porous model is a reduced hydrodynamic load. In turn, this will mitigate the bending stress experienced by the skeletal system, thereby further contributing to its exceptional mechanical stability that has been so far attributed solely to its mechanical properties [4]. To quantify the hydrodynamic loading experienced by the models, we computed the drag coefficient C_D:

$$C_D = \frac{2\overline{F}_{\mathrm{drag}}}{A\rho_{\mathrm{inlet}}\, u_{\mathrm{inlet}}^2}, \tag{1}$$

where $\overline{F}_{\mathrm{drag}}$ is the total (average) drag force acting on the model, computed at the statistical steady-state and along the flow direction; ρ_{inlet} and u_{inlet} are the fluid density and speed at the domain inlet, respectively; A is the area of the transverse section of the model, perpendicular to the fluid flow (the value $A = DH$ for P1 and S1 is modified for P2 and S2 to account for helical ridges). The values of C_D are reported in Fig. 3c. Predictably, the presence of the *fenestræ* on the surface of *E. aspergillum* yields a remarkable drag reduction, evident for $\mathrm{Re} \geq 500$. On the other hand, the helical ridges introduce a systematic drag increase, which, however, does not mitigate the benefits provided by the *fenestræ* (see Fig. 3c). These results are robust with respect to the presence of local defects, which are responsible for a modest drag reduction from 2.5 to 3.5% (see Extended Data Fig. 6). Since drag reduction is often a goal of sessile aquatic organisms to reduce deformation

and prevent breakage [38], the presence of the ridges introduces a new question as to whether they exclusively serve structural functions, as those identified in [3]. We propose that this is not the case, with the helical ridges regulating a trade-off between drag reduction and feeding and reproductive functions.

In contrast with shallow-water sponges that have access to highly nutritious photosynthetic algae, deep-sea sponges feed mainly on non-photosynthetic bacteria that are suspended at low concentrations in the water column [39]. Feeding is particularly challenging in the habitat of deep-sea sponges, where strong currents favor the presence of clay and detritus (making up more than 97% of suspended particles). *E. aspergillum* accomplishes highly effective, selective filter feeding [13], through low-speed vortical structures within its body cavity, which are evidenced in Fig. 1c. These complex swirling patterns favor the distribution of suspended particles throughout the flagellated chambers of the sponge, where nutrients are absorbed and inorganic particles are discarded. Similarly, the reproduction of *E. aspergillum* is likely enhanced through the swirling patterns within the body cavity. Sexual reproduction is known to occur in this species, in which free–spawned sperm fertilize retained eggs [14, 22]: vortical structures could thus favor the encounter between gametes within the body cavity.

To quantify the extent to which the helical ridges of *E. aspergillum* contribute to the generation of these low-speed vortical structures within the body cavity, we contrasted the flow physics fields of the two porous models (P1 versus P2). Such a comparison was carried out in terms of the vorticity magnitude and the *Q-criterion*, which defines a vortex as a flow region where

$Q = \frac{1}{2}(||\bar{\Omega}||^2 - ||\bar{S}||^2) > 0$, where $\bar{\Omega}$ and $\bar{S}$ are the skew-symmetric and symmetric parts of the velocity gradient tensor [32, 33, 40] (see Fig. 4 and Methods for further details). According to such a criterion, $Q > 0$ implies that the energy connected to local fluid rotation prevails over dissipative phenomena, such that vortical structures may arise within the flow. Figure 4a provides evidence of a magnifying effect of the helical ridges on the generation of swirling patterns within the body cavity. From the enstrophy, we further estimated the residence time within the body cavity, as a measure of the time available for suspended nutrients and sperm to dwell within the sponge body cavity. The presence of the helical ridges is responsible for increasing the mean residence time and widening its distribution, thereby increasing the time available for feeding and sexual reproduction.

We capitalized on the versatility of numerical simulations to isolate the fluid dynamic role of each skeletal motif of *E. aspergillum*. Using an entire specimen of *E. aspergillum* as a reference, we performed a series of morphological manipulations within an *in-silico* experimental campaign on one of the world-wide leading edge computational facilities, CINECA's "Marconi100". For all the models under inspection, we investigated different flow regimes, using data on water viscosity and velocity distributions on the bottom of the seafloor, for depths of $100 - 1000$ m, summarised by the Reynolds numbers $\mathrm{Re} = 100,\ 500,\ 1000,\ 1500$, and 2000.

Overall, our computational results reveal a rich, multifaceted role of the skeletal motifs of *E. aspergillum* on the flow physics within and beyond its body cavity. Skeletal motifs play a critical role on the functional ecology of this species, beyond the previously known benefits to its mechanical properties. More specifically, the presence of the *fenestræ* blows the intermittency

rising at flow regimes at $\mathrm{Re} > 100$, several diameters downstream the organism, thereby providing a reduction in the drag, which mitigates the stress experienced by the sponge and improve its mechanical stability. The helical ridges that decorate the surface of the sponge promote vortical structures within the body cavity that increase the available time for the sponge to feed and sexually reproduce, at the cost of a secondary increase in the drag.

Our results unveil mechanisms of extraordinary adaptation to live in the abyssal, laying the foundations for a new class of computational investigations at the intersection between fluid mechanics, organism biology, and functional ecology.

References

1. Owen, R., Description of a new genus and species of sponge (*Euplectella aspergillum*, O.). *Transactions of the Zoological Society of London*, **3**(2), 203-215 (1849).

2. Report on the scientific results of the voyage of H.M.S. Challenger during the years 1873-76 - under the command of Captain George S. Nares, R.N., F.R.S. and Captain Frank Turle Thomson, R.N. (1887), v. XXI - Zoology, Plates. https://archive.org/details/reportonscientif21grea/page/n13/mode/2up.

3. Weaver, J.C., Aizenberg, J., Fantner, G.E., Kisailus, D., Woesz, A., Allen, P., Fields, K., Porter, M.J., Zok, F.W., Hansma, P.K. and Fratzl, P., Hierarchical assembly of the siliceous skeletal lattice of the hexactinellid sponge *Euplectella aspergillum*. *Journal of Structural Biology*, **158**(1), 93-106 (2007).

4. Aizenberg, J., Weaver, J.C., Thanawala, M.S., Sundar, V.C., Morse, D.E. and Fratzl, P., Skeleton of *Euplectella sp.*: structural hierarchy from the nanoscale to the macroscale. *Science*, **309**(5732), 275-278 (2005).

5. Monn, M.A., Weaver, J.C., Zhang, T., Aizenberg, J. and Kesari, H., New functional insights into the internal architecture of the laminated anchor spicules of *Euplectella aspergillum*. *Proceedings of the National Academy of Sciences*, **112**(16), 4976-4981 (2015).

6. Fernandes, M.C., Aizenberg, J., Weaver, J.C. and Bertoldi, K., Mechanically robust lattices inspired by deep-sea sponges. *Nature Materials*, 1-5 (2020).

7. Succi, S., The lattice Boltzmann equation: for complex states of flowing matter. Oxford University Press (2018).

8. Kanari, S.-I., Kobayashi, C. and Ishikawa, T., An estimate of the velocity and stress in the deep ocean bottom boundary layer, *Journal of the Faculty of Science, Hokkaido University, Series 7, Geophysics*, **9**(1), 1-16 (1991), http://hdl.handle.net/2115/8778.

9. Doron, P., Bertuccioli, L., Katz, J. and Osborn, T.R., Turbulence characteristics and dissipation estimates in the coastal ocean bottom boundary layer from PIV data. *Journal of Physical Oceanography*, **31**(8), 2108-2134 (2001).

10. https://ittc.info/media/4048/75-02-01-03.pdf

11. Nayar, K.G., Sharqawy, M.H. and Banchik, L.D.. Thermophysical properties of seawater: A review and new correlations that include pressure dependence. Desalination, **390**, 1-24 (2016).

12. http://web.mit.edu/seawater

13. Yahel, G., Eerkes-Medrano, D.I. and Leys, S.P., Size independent selective filtration of ultra-plankton by hexactinellid glass sponges. *Aquatic Microbial Ecology*, **45**(2),181-194 (2006).

14. Schulze, F.E., XXIV.—On the structure and arrangement of the soft parts in *Euplectella aspergillum. Earth and Environmental Science Transactions of The Royal Society of Edinburgh*, **29**(2), 661-673 (1880).

15. Kitano, H. Computational systems biology, *Nature* **420**(6912), 206-210 (2002).

16. Coveney, P.V., Boon, J.P. and Succi, S. Bridging the gaps at the physics–chemistry–biology interface. *Philosophical Transactions of the Royal Society A: Mathematical, Physical and Engineering Sciences* **374** 20160335 (2016).

17. Succi, S., Amati, G., Bernaschi, M., Falcucci, G., Lauricella, M. and Montessori, A. Towards exascale lattice Boltzmann computing. *Computers & Fluids*, **181**, 107-115 (2019).

18. Fung, Y.C., Biomechanics: mechanical properties of living tissues. Springer Science & Business Media (2013).

19. https://www.hpc.cineca.it/hardware/marconi100

20. Reitner, J. and Mehl, D., Early paleozoic diversification of sponges; new data and evidences. *Geologisch-paläontologische Mitteilungen, Innsbruck*, **20**, 335-347 (1995).

21. Moore, T.J., XXVIII.—On the habitat of the Regadera (watering-pot) or Venus's flower-basket (*Euplectella aspergillum, Owen*). *Journal of Natural History*, **3**(15), 196-199 (1869).

22. Leys, S.P., Mackie, G.O. and Reiswig, H.M., The biology of glass sponges. *Advances in Marine Biology*, **52**, 1-145 (2007).

23. Gray, J.E., LXIV.—Venus's flower-basket (Euplectella speciosa). *Annals and Magazine of Natural History*, **18**(108), 487-490 (1866).

24. Saito, T., Uchida, I. and Takeda, M., Skeletal growth of the deep-sea hexactinellid sponge Euplectella oweni, and host selection by the symbiotic shrimp Spongicola japonica (Crustacea: Decapoda: Spongicolidae). *Journal of Zoology*, **258**(4), 521-529 (2002).

25. Chree, C., Recent Advances in our Knowledge of Silicon and of its Relations to Organised Structures. *Nature* **81**, 206–208 (1909).

26. Woesz, A., Weaver, J.C., Kazanci, M., Dauphin, Y., Aizenberg, J., Morse, D.E. and Fratzl, P., Micromechanical properties of biological silica in skeletons of deep-sea sponges. *Journal of Materials Research*, **21**(8), 2068-2078 (2006).

27. Monn, M.A., Vijaykumar, K., Kochiyama, S. and Kesari, H., Lamellar architectures in stiff biomaterials may not always be templates for enhancing toughness in composites. *Nature Communications*, **11**(1), 1-12 (2020).

28. Vogel, S., Current-induced flow through living sponges in nature. *Proceedings of the National Academy of Sciences*, **74**(5), 2069-2071 (1977).

29. Prandtl, L., Applied hydro- & aeromechanics. By: OG Tietjens, Translated by: JP Den Hartog, Dover Publications Inc., New York (1957).

30. Tritton, D.J., Physical Fluid Dynamics, 2nd edn. Clarendon (1988) - Chapter 21, "Turbulent Shear Flows".

31. Gualtieri, P., Casciola, C.M., Benzi, R., Amati, G. and Piva, R., Scaling laws and intermittency in homogeneous shear flow. *Physics of Fluids*, **14**(2), pp.583-596 (2002).

32. Hunt, J. C. R., Wray, A. and Moin, P., Eddies, stream, and convergence zones in turbulent flows. Center for Turbulence Research Report CTR-S88 (1988).

33. Haller, G., An objective definition of a vortex. *Journal of Fluid Mechanics*, **525** (2005).

34. Kawamura, T., Takami, H. and Kuwahara, K., Computation of high Reynolds number flow around a circular cylinder with surface roughness. *Fluid Dynamics Research*, **1**(2), 145 (1986).

35. Hanchi, S., Askovic, R. and Ta Phuoc, L., Numerical simulation of a flow around an impulsively started radially deforming circular cylinder. *International Journal for Numerical Methods in Fluids*, **29**(5), 555-573 (1999).

36. Sahin, M. and Owens, R.G., A numerical investigation of wall effects up to high blockage ratios on two-dimensional flow past a confined circular cylinder. *Physics of Fluids*, **16**(5) (2004).

37. Fujisawa, N., Tanahashi, S. and Srinivas, K., Evaluation of pressure field and fluid forces on a circular cylinder with and without rotational oscillation using velocity data from PIV measurement. *Measurement Science and Technology*, **16**(4), 989 (2005).

38. Koehl, M.A.R., How do benthic organisms withstand moving water? *American Zoologist*, **24**(1), 57-70 (1984).

278 39. Yahel, G., Whitney, F., Reiswig, H.M., Eerkes-Medrano, D.I. and Leys, S.P., In situ feeding
279 and metabolism of glass sponges (Hexactinellida, Porifera) studied in a deep temperate fjord
280 with a remotely operated submersible. *Limnology and Oceanography*, **52**(1), 428-440 (2007).

281 40. Krastev, V.K., Amati, G., Succi, S. and Falcucci, G., On the effects of surface corrugation on
282 the hydrodynamic performance of cylindrical rigid structures. *The European Physical Journal*
283 *E*, **41**(8) (2018).

284 41. Krüger, T., Kusumaatmaja, H., Kuzmin, A., Shardt, O., Silva, G. and Viggen, E.M., The lattice
285 Boltzmann method. Springer International Publishing (2017).

286 42. Montessori, A. and Falcucci, G., Lattice Boltzmann modeling of complex flows for engineer-
287 ing applications. Morgan & Claypool Publishers (2018).

288 43. Johnson, R.W. (Ed.), Handbook of fluid dynamics. CRC Press (2016).

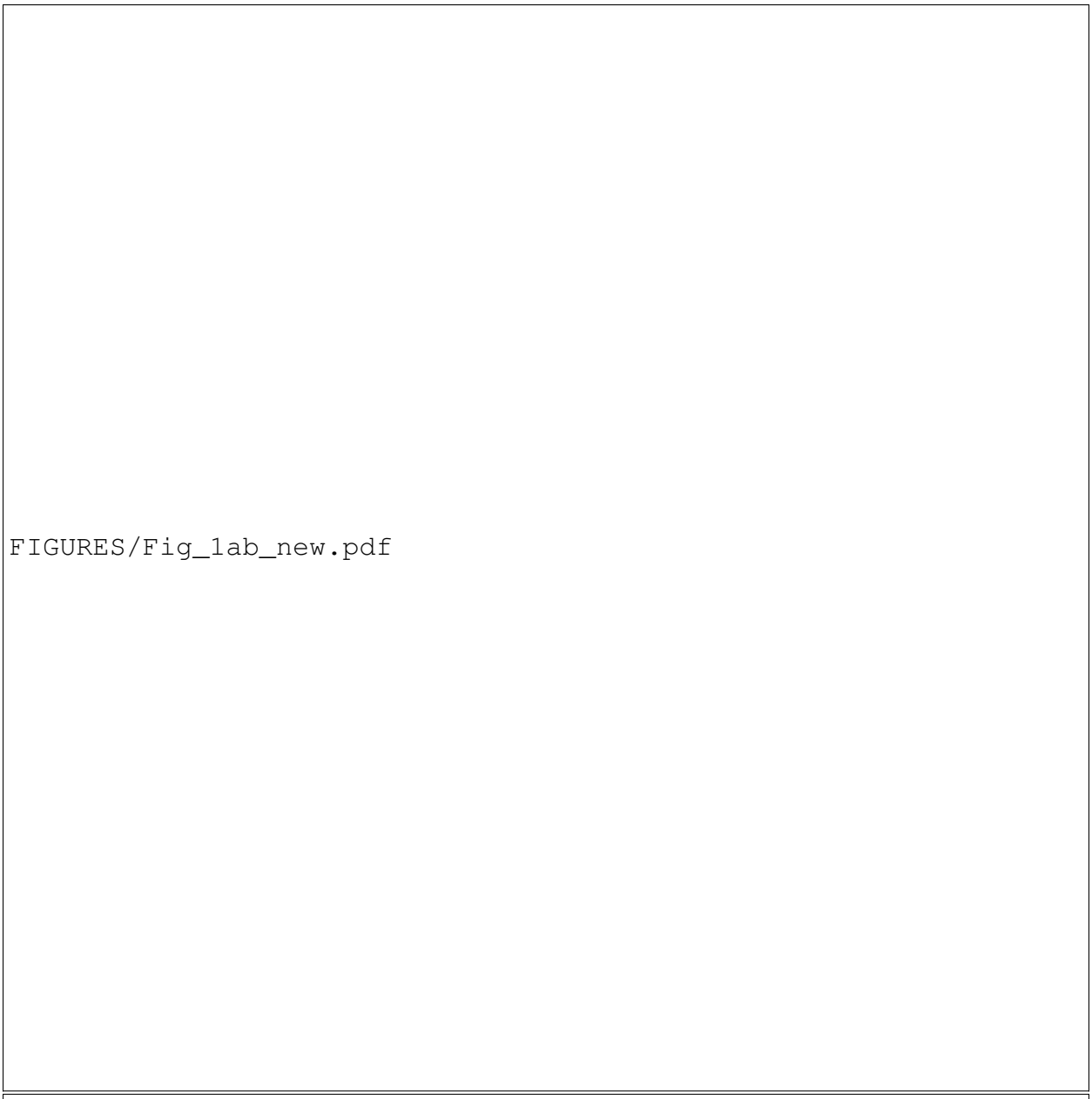
FIGURES/Fig_1ab_new.pdf

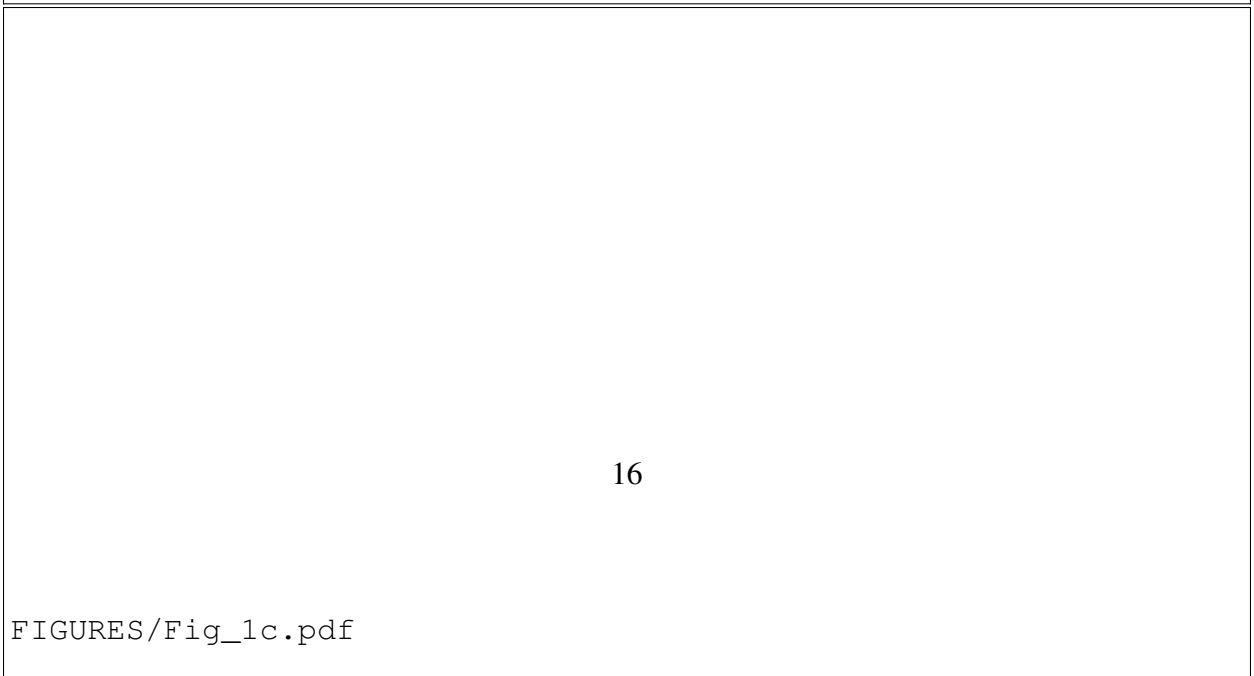
FIGURES/Fig_1c.pdf

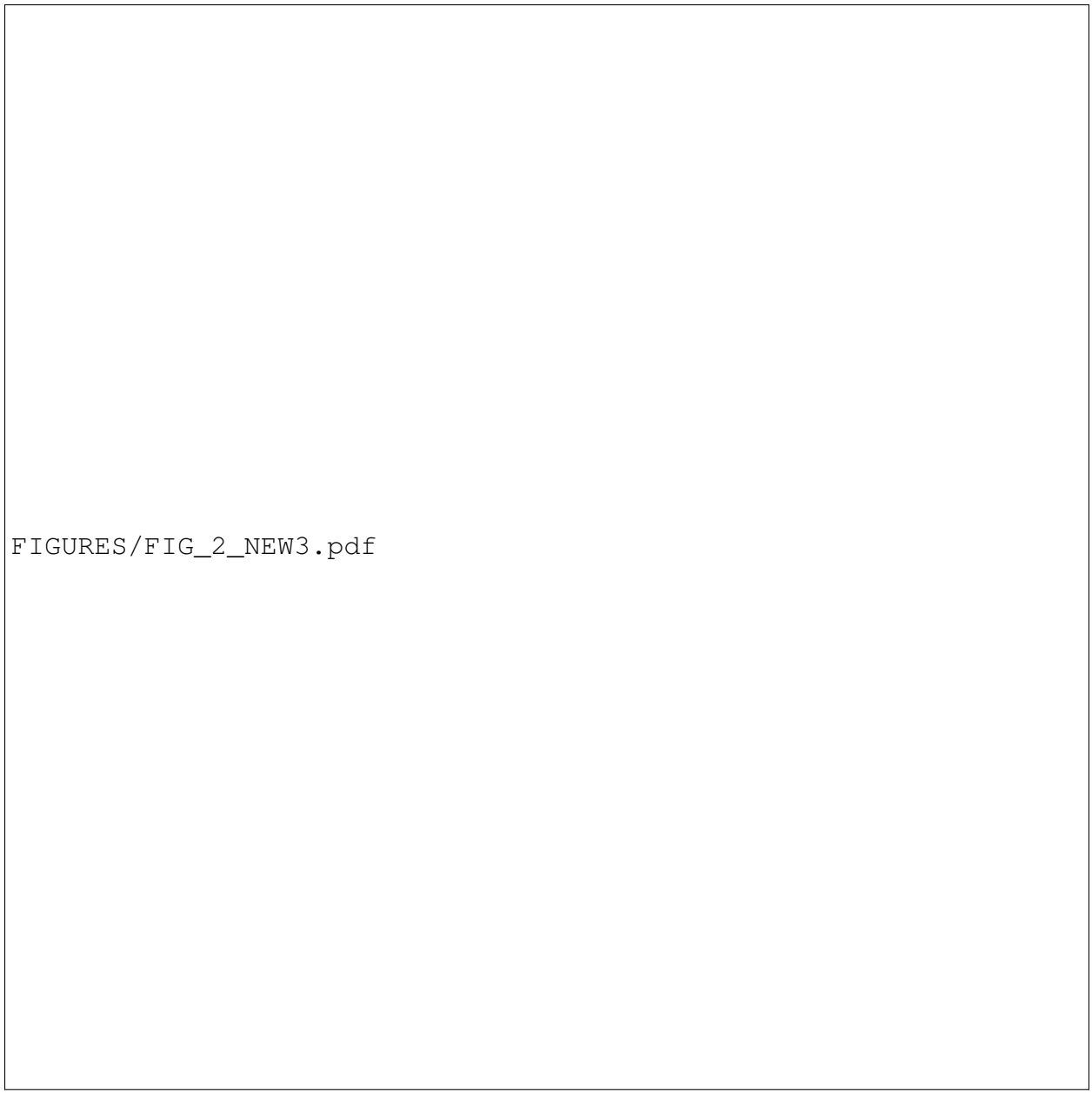

Figure 2: **Effect of manipulations of the morphology of *E. aspergillum* on the flow downstream**. **a**: Time evolution of the three components of the flow velocity $\vec{u}(P,t)$, where P is a probe located 2.5 diameters downstream the model, at $\mathrm{Re} = 2000$, for the four considered, periodic geometries. The comparison of the velocity components at P for the different models confirms the abating effect of the skeletal motifs of *E. aspergillum* on flow fluctuations downstream the sponge. The panels report the last $\sim 1\%$ of the whole simulation time span (5×10^4 out of 5.2×10^6 time steps, corresponding to the last ~ 20 s of the simulated time). Data include statistical variations due to local defects (solid lines are mean values, and shaded regions identify minima and maxima). **b**: Polar diagrams of the x, y velocity components in [cm/s], downstream the model, at probe location P, for all explored Re regimes. The panel highlights the stabilising effects on the fluid wake, due to the concurrent influence of the *fenestræ* and the ridges of *E. aspergillum*.

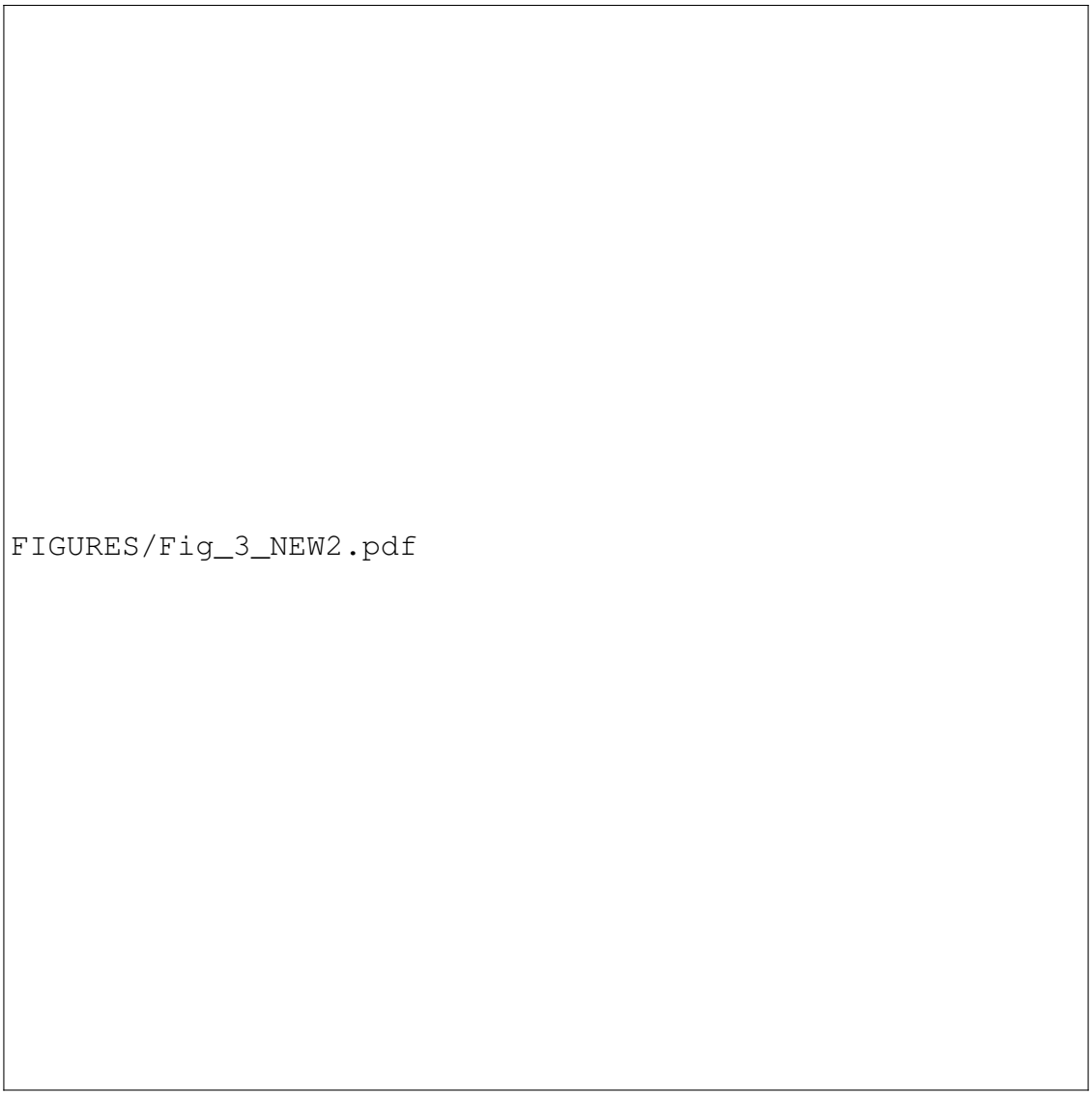

Figure 3: **Effect of manipulations of the morphology of *E. aspergillum* on helicity, enstrophy, and drag coefficient.** **a**: Helicity $\mathcal{H}$ (upper part of the panel) and enstrophy $|\vec{\omega}|^2$ (lower part of the panel) fields at $\mathrm{Re} = 2000$ for the plain cylinder (S1) and the hollow cylindrical lattice with helical ridges (P2). **b**: Zoomed-in view of helicity and enstrophy along the x direction in the centerline of the domain for the S1 and P2 at $\mathrm{Re} = 2000$; data include statistical variations due to local defects (solid lines are mean values, and shaded regions identify minima and maxima). The dashed circle identifies the model and the black markers the nearly quiescent region that forms downstream P2, due to its *fenestræ* and the external ridges. **c**: Drag coefficient C_D for all the simplified models, compared to literature values for cylinders [34–37]; the comparison at $\mathrm{Re} = 100$ supports the accuracy of the simulations (further validation can be garnered from the Strouhal number; see Methods and Extended Data Table 1). The panel highlights the beneficial role of the *fenestræ* and the detrimental role of the helical ridges on the drag experienced by the models: the hollow cylindrical lattice with helical ridges offers the second smallest drag coefficient, after the hollow cylindrical lattice. Notably, the helical ridges contribute a reduction of in-plane transverse force, but peak-to-peak oscillations are secondary with respect to the drag force (see Methods and Extended Data Fig. 6).

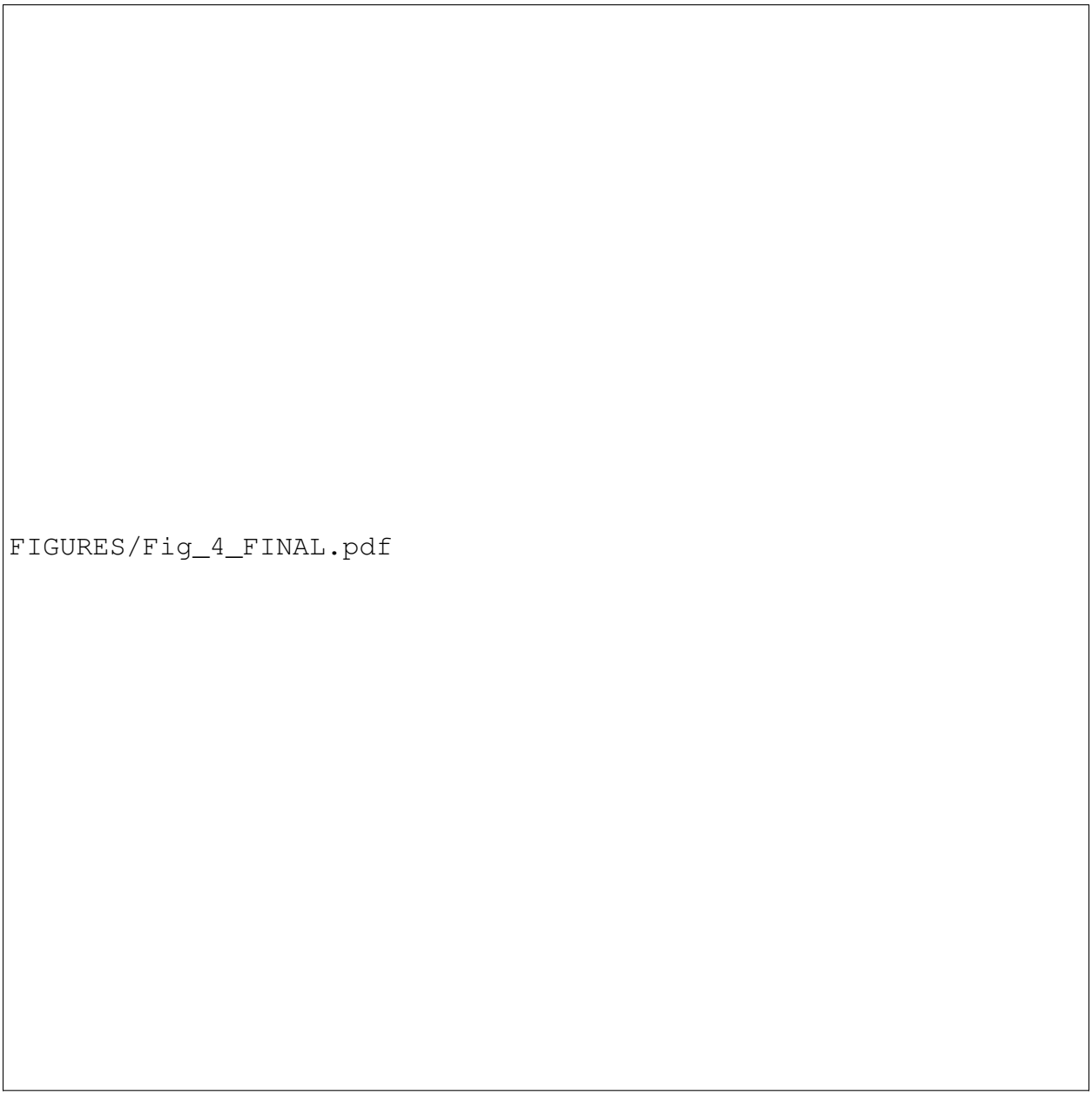

Figure 4: **Role of the ridges on flow speed, vorticity, *Q*-structures, and residence time within the body cavity. a**. Flow speed, vorticity, and Q-structures for the two porous models, without and with helical ridges (P1: top, and P2: bottom). The upper part of each panel reports the streaklines colored according to the flow speed, while the lower part shows contours of the vorticity magnitude $|\vec{\omega}|$ along with regions characterised by $Q > 0$ (vortical structures). The panels help visualizing the hydrodynamic role of the external ridges in amplifying vortical structures within the *E. aspergillum*'s body cavity, promoting selective filter feeding and gamete encounter for sexual reproduction. **b**. Distribution of the non-dimensional residence time within the body cavity, $t^* = \frac{|\mathcal{H}| \, D}{u_{\text{inlet}}^2}$; data include statistical variations due to local defects (solid lines are mean values and error bars identify minima and maxima). The panel highlights the effect of the external ridges in extending the tails of the distribution, thereby granting more time to the organism to feed and sexually reproduce.

Methods

Reconstruction of the skeletal system of *E. aspergillum*. The skeletal system of this organism comprises four main regions: the anchoring bulb, the curved section connecting the bulb to the main body, the main body, and the terminal sieve plate at the apex, called *osculum* (links to high-resolution photographs and images of *E. aspergillum* can be found in [45–48]; further images are in Extended Data Figs. 2, 3, 7, and 8). We realised a digital mock-up of the complete geometry, as reported in Extended Data Fig. 7, by accurately reproducing all its main characteristics in SolidWorks® and MeshLab®. Excluding the solid anchoring bulb, the remaining regions consist of a periodic lattice of two intersecting patterns. The main pattern is composed of axial and circumferential filaments with a diameter of 0.5 mm, orthogonally crossing each other. The secondary pattern is characterised by smaller ligaments with a diameter of 0.2 mm and is arranged at 45° with respect to the main pattern.

The lattice envelops a cylinder of 40 mm in diameter that defines the main body section and bends into a cone-like shape that represents the connecting region to the anchoring bulb. A non-periodic arrangement of 5 mm-thick helical ridges is placed on the outer surface of the lattice. Ridges are organized in a sequence of rows along the secondary pattern of the lattice, with intersecting helical patterns and random interruptions according to the literature [3]; simulations on this complete geometry are in Fig. 1c.

Along with the detailed reconstruction of *E. aspergillum*'s skeletal system, four simplified models of the main body were generated (see Fig. 1b) to assess the effect of morphological ma-

nipulations on the flow physics, namely, a plain cylinder (S1), a plain cylinder with helical ridges (S2), a hollow cylindrical lattice (P1), and a hollow cylindrical lattice with helical ridges (P2); simulations on these models are in Figs. 2a, 2b, 3a, 3b, 3c, 4a, and 4b.

Extended Data Fig. 2 demonstrates a lattice site resolution within the *fenestræ* of the secondary ligament pattern of the hollow cylindrical lattice with helical ridges (and its manipulations) of $\sim 5 \times 5$ lattice sites, which is sufficient for the resolution of the hydrodynamics with the Lattice Boltzmann method [49]. More specifically, for the method to be reliable, the mean free path λ should be much smaller than the lattice spacing, so that $\lambda = c_s \left(\tau - \frac{1}{2}\right) \ll 1$, with c_s being the lattice sound speed and τ the characteristic time scale toward local relaxation. For $\mathrm{Re} = 2000$, we have $\nu = 0.01$, corresponding to $\tau = 0.5033$, which implies that in the ~ 5 grid points of the side of the *fenestra*, fluid particles collide $O(100)$ times, thereby ensuring the hydrodynamic regime through the hole.

Beyond the validation of our predictions on drag coefficients at $\mathrm{Re} = 100$ in Fig. 3c, we garnered further evidence through the analysis of the wake downstream the plain cylinder model (S1). More specifically, we examined the Strouhal number, $\mathrm{St} = \frac{\mathcal{F}\, D}{u_{\mathrm{inlet}}}$, where $\mathcal{F}$ is the frequency of the downstream vortex shedding (evaluated at the probe P location), D is the model characteristic length (that is, the diameter), and u_{inlet} the inlet velocity magnitude. Extended Data Table 3 summarizes the comparison between our predictions of St at different Re against experimental measurements from [50]. The Table demonstrates the accuracy of our numerical predictions, with an error ε ranging between 3.8% and 6.3%.

Generation of random defects in the geometry. Taking advantage of the versatility of our numerical method to explore models of arbitrary complexity, we generated nine variations of the hollow cylindrical lattice with helical ridges (see Fig. 1b). These variations were obtained by applying random morphological defects in the skeletal motifs that simulate wounds and scars, which have been widely documented [22]. Wounds were simulated by removing filaments and portions of ridges in the pristine model; on the contrary, scars were represented as added masses to the lattice and the ridges (see Extended Data Fig. 4).

The mass of the model was kept constant across variations, which accounted for a $\sim 5\%$ mass redistribution. The rationale for this selection is grounded in the literature [22], which indicates that these organisms can regenerate no more than 10% of their skeletal system when damaged, while overcoming such a threshold would lead to death. We report the nine variations of the hollow cylindrical lattice with helical ridges (P2) that were obtained by applying random morphological defects in Extended Data Fig. 4. We performed extreme fluid dynamic simulations for these nine variations, covering all the considered Re (namely, $\mathrm{Re} = 100, 500, 1000, 1500$, and 2000). The dataset was used to ascertain statistical variations on the drag coefficient C_D, the non-dimensional residence time t^*, and helicity $\mathcal{H}$ and enstrophy $|\vec{\omega}|^2$ within the computational domain.

The Lattice Boltzmann method: boundary conditions and turbulence evaluation. The fluid fields evolve in time according to the following Lattice Boltzmann (LB) equation:

$$f_i(\boldsymbol{x} + \boldsymbol{c}_i, t+1) - f_i(\boldsymbol{x}, t) = \omega[f_i^{\mathrm{eq}}(\boldsymbol{x}, t) - f_i(\boldsymbol{x}, t)]\,, \tag{2}$$

where $f_i(\boldsymbol{x}, t)$ represents the probability density function of finding a fluid particle at site $\boldsymbol{x}$ and discrete time t, moving along the i-th lattice direction, and f_i^{eq} identifies local Maxwellian equilibrium. In the present work, we employed a 19 discrete speed ($i = 0, ..., 18$) scheme along the three spatial dimensions, also known as D3Q19 lattice. For details on the method, we refer to [7, 41, 42, 44].

One of the main advantages of the LB method is the handling of complex geometries, such as the one of the *E. aspergillum* under investigation. Leveraging the discrete Cartesian nature of the method, it is possible to implement second-order accurate boundary conditions by using the algorithms proposed in [7, 42]. Here, we impose the following boundary conditions:

- *Inflow*: we fix the velocity magnitude based on the desired Re [42];
- *Outflow*: we impose a zero-gradient condition, by copying the density and velocity from the last fluid plane into the boundary outlet buffer [42];
- *Side boundaries*: we use periodic boundary conditions;
- *Internal boundaries*: we impose no-slip boundary conditions via the standard bounce-back procedure. This condition is applied to the solid nodes of the geometries (S1, S2, P1, P2, and complete model of *E. aspergillum*). The same no-slip boundary conditions are also employed for the seafloor in the study of the complete model; and
- *Top-bottom boundaries*: We use periodic boundary conditions for all geometries, except of the complete one, for which we enforce no-slip on the bottom and free-slip on the top.

To examine the flow physics inside the body cavity and in the downstream wake of the considered geometries, we studied the flow vorticity $\vec{\omega}$, enstrophy $|\vec{\omega}|^2$, and helicity $\mathcal{H}$. Through these quantities, we identified the presence of vortical structures via the Q-criterion [33], and we estimated the non-dimensional residence time within the body cavity; more details on these computations can be found in [43]. For the sake of completeness, below we report the definitions of the various fluid parameters employed.

Enstrophy is given by

$$|\vec{\omega}|^2 = |\,\vec{\nabla} \times \vec{u}\,|^2 = \left(\frac{\partial u_z}{\partial y} - \frac{\partial u_y}{\partial z}\right)^2 + \left(\frac{\partial u_x}{\partial z} - \frac{\partial u_z}{\partial x}\right)^2 + \left(\frac{\partial u_y}{\partial x} - \frac{\partial u_x}{\partial y}\right)^2 , \tag{3}$$

whereas helicity is computed as

$$\mathcal{H} = \vec{u} \cdot \left(\vec{\nabla} \times \vec{u}\right) = u_x \left(\frac{\partial u_z}{\partial y} - \frac{\partial u_y}{\partial z}\right) + u_y \left(\frac{\partial u_x}{\partial z} - \frac{\partial u_z}{\partial x}\right) + u_z \left(\frac{\partial u_y}{\partial x} - \frac{\partial u_x}{\partial y}\right). \tag{4}$$

Helicity in the body cavity is in turn used to estimate the non-dimensional residence time.

To compute the Q-criterion, we separated the anti-symmetric (vorticity tensor) and symmetric (rate-of-strain tensor) components of the velocity gradient tensor, defined as follows:

$$\bar{\Omega} = \frac{1}{2}\left[\nabla\vec{u} - (\nabla\vec{u})^{\mathrm{T}}\right] = \frac{1}{2}\left(\frac{\partial u_\alpha}{\partial x_\beta} - \frac{\partial u_\beta}{\partial x_\alpha}\right), \tag{5}$$

$$\bar{S} = \frac{1}{2}\left[\nabla\vec{u} + (\nabla\vec{u})^{\mathrm{T}}\right] = \frac{1}{2}\left(\frac{\partial u_\alpha}{\partial x_\beta} + \frac{\partial u_\beta}{\partial x_\alpha}\right), \tag{6}$$

where T indicates tensor transposition and Greek subscripts α, β label the Cartesian components.

Finally, the Q factor, is defined as

$$Q = \frac{1}{2}\left[||\bar{\Omega}||^2 - ||\bar{S}||^2\right] , \tag{7}$$

where the symbol $||\cdot||$ denotes tensorial norm. Positive Q's identify flow regions where rotational energy exceeds dissipation, thereby setting the stage for the emergence of vortical structures. High helicity, on the other hand, associates with the presence of three-dimensional spiraling structures.

Extended Data Table 2 reports the main physical and computational parameters, including information about the conversion between lattice and physical units.

High-Performance-Computing. Simulations were carried out on two supercomputing facilities at CINECA, namely, "Marconi" and "Marconi100". The former is a CPU based architecture, while the latter, ranking 9th in the May 2020 Top500 list [19], is based on GPU accelerators. Simulations on S1, S2, and P1 were performed on "Marconi", involving 128 tasks and 64 threads for each task, for a total of $8,192$ cores used. These are the least expensive runs among those we performed, yielding 0.7 PFLOPS (Peta Floating Point Operations per Second) peak performance and exploiting $\sim 4\%$ of the CPU-based HPC facility. Simulations on P2 and its nine variations with random defects were performed on "Marconi100". Each run used 16 Compute Nodes (CN): each CN has 32 IBM Power9 cores and 4 Nvidia V100 GPUs (with 80 Streaming Multiprocessors (SMs) per GPU). All the simulations on the complete model of *E. aspergillum* were run on 128 CN of "Marconi100", involving $1/8$ of the entire HPC facility and yielding ~ 4 PFLOPS of peak performance. The simulations on the complete model required $4,096$ CPU cores and $40,960$ SMs,

on a domain characterized by $O(100 \times 10^9)$ grid points for $\sim 5 \times 10^6$ time steps.

The overall computational effort for all the simulations presented in this study resulted into $O(10^2)$ Terabytes of raw data, and it required $\sim 75,000$ GPU hours and $\sim 2,000,000$ CPU hours. Extended Data Table 3 summarizes the architecture and computational resources of the study. The excellent scalability of the LB method on the aforementioned computational architecture proved instrumental to enable the full-scale simulation of *E. aspergillum*, from microscopic geometric details, all the way up to the entire organism.

Supporting fluid dynamics analyses Simulation results on vorticity magnitude for all Re are presented in Extended Data Fig. 5 to verify the formation of a nearly-quiescent region downstream the porous models at $\mathrm{Re} \geq 500$. A zoomed-out view of Fig. 3c with error bars associated with the minimum and maximum values is shown in Extended Data Fig. 6 to assess statistical variations in the prediction of the drag coefficient due to the random defects.

Along with the drag coefficients, we also considered the lift coefficient, defined as

$$C_L = \frac{2F_{\mathrm{lift}}}{A\rho_{\mathrm{inlet}}\, u_{\mathrm{inlet}}^2}, \tag{8}$$

where F_{lift} is the time-varying in-plane transverse force experienced by the models. For $\mathrm{Re} = 2000$, we report in Extended Data Fig. 9, the time trace at statistical steady-state of the lift coefficient.

Data availability

STL files for all the models, raw data for the plots, and scripts to reproduce the Figures are available on GitHub at https://github.com/giacomofalcucci/Euplectella_HPC. Additional data that support the findings of this study are available from the corresponding author on request.

Code availability

All codes necessary to reproduce results in main paper are available on GitHub at https://github.com/giacomofalcucci/Euplectella_HPC.

References

44. Falcucci, G., Ubertini, S., Biscarini, C., Di Francesco, S., Chiappini, D., Palpacelli, S., De Maio, A. and Succi, S. Lattice Boltzmann methods for multiphase flow simulations across scales. *Communications in Computational Physics*, **9**(2), 269-296 (2011).

45. https://commons.wikimedia.org/wiki/File:Euplectella-aspergillum.jpg;

46. https://asknature.org/strategy/glass-skeleton-is-tough-yet-flexible/;

47. https://www.researchgate.net/figure/Euplectella-Aspergillum_fig1_344450084;

48. http://www.microscopy-uk.org.uk/mag/indexmag.html?http://www.microscopy-uk.org.uk/mag/artfeb12/rh-euplectella4.html.

49. Succi, S., The lattice Boltzmann equation: for fluid dynamics and beyond. Oxford University Press (2001)

50. Norberg, C., An experimental investigation of the flow around a circular cylinder: influence of aspect ratio. *Journal of Fluid Mechanics*, **258**, 287-316 (1994)

Acknowledgments G.F wishes to acknowledge the CINECA Computational Grant ISCRA-B IsB17 - "SPONGES", id. HP10B9ZOKQ and, partially, the support of PRIN Projects CUP E82F16003010006 (G.F. Scientific Responsible for Tor Vergata Research Unit) and CUP E84I19001020006 (Prof. Gino Bella Scientific Responsible). G.P. acknowledges the support of the Forrest Research Foundation. M.P. would like to acknolwegde the support of the National Science Foundation under grant no. CMMI 1901697. S.S. wishes to acknowledge financial support from the European Research Council under the Horizon 2020 Programme Advanced Grant Agreement n. 739964 ("COPMAT"). G.F. and S.S. wish to kindly acknowledge Prof. Katia Bertoldi, Dr. Matheus C. Fernandes, and Dr. James C. Weaver for introducing them to the marvels of *E. aspergillum* and for early discussions on the subject. Prof. Andrea Luigi Facci from Tuscia University is kindly acknowledged for providing precious help with Figure realization. Prof. Efthimios Kaxiras from Harvard University is kindly acknowledged for early discussions that proved fruitful for the development of the present code.

Author contributions G.F. designed the research; G.F and G.A. wrote the original LB method code; G.A. extended the code for massively parallel computation, developed the GPU version for "Marconi100", and helped collect and post-process the data; P.F. realized all the models; V.K.K. run the validation tests and helped in post-processing and data interpretation; G.F. created the Figures; G.P. and M.P. led the biological framing of the results; G.F., M.P., and S.S. supervised the research and interpretation of the results; G.F.,

G.P., M.P., and S.S. wrote the manuscript. All authors contributed in analyzing the results of the simulations and revising the manuscript.

Competing Interests The authors declare that they have no competing financial interests.

Correspondence Correspondence and requests for materials should be addressed to Giacomo Falcucci (email: giacomo.falcucci@uniroma2.it; falcucci@g.harvard.edu).

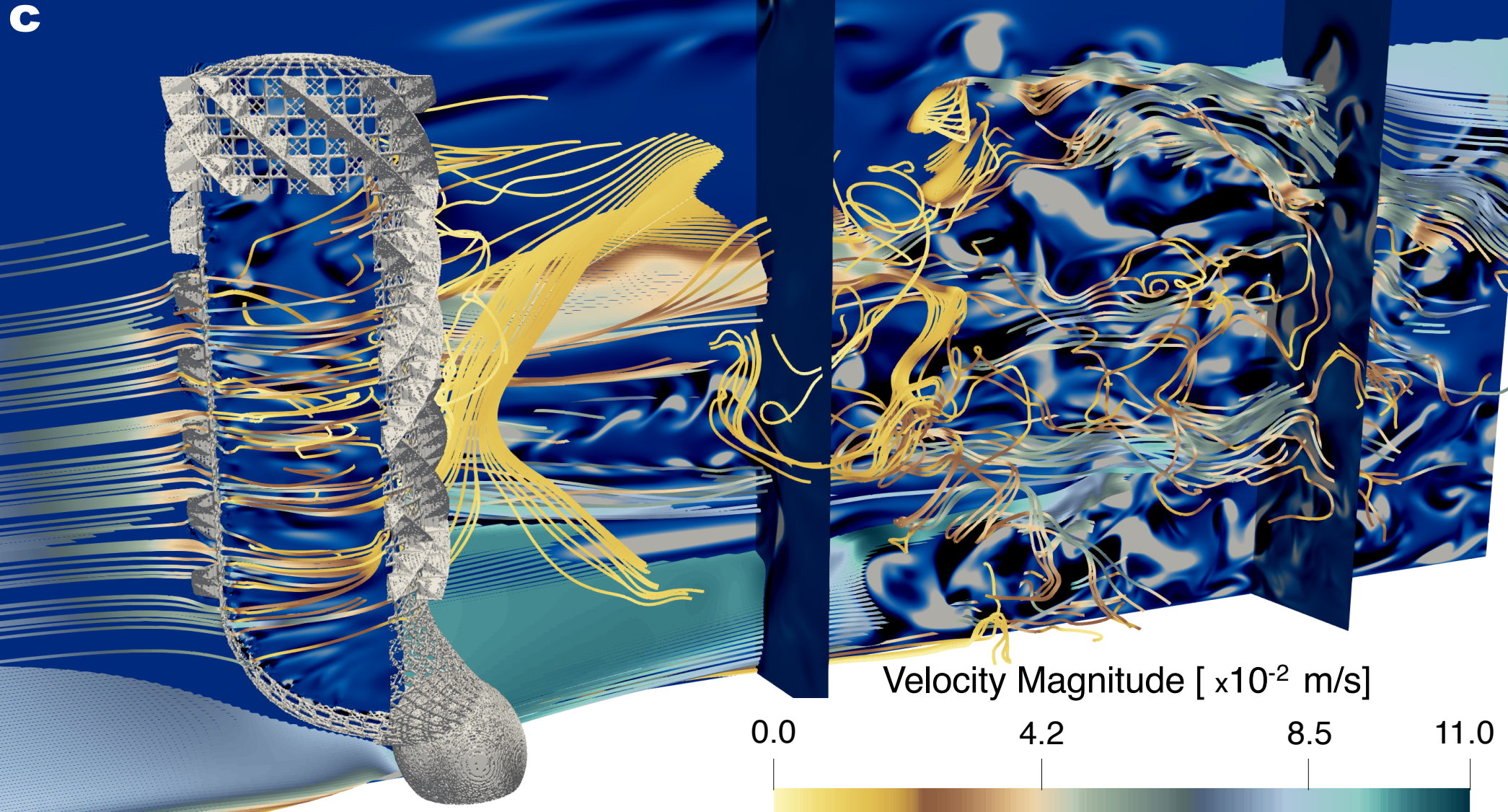
c
Velocity Magnitude [x10-2 m/s]
0.0
4.2
8.5
11.0

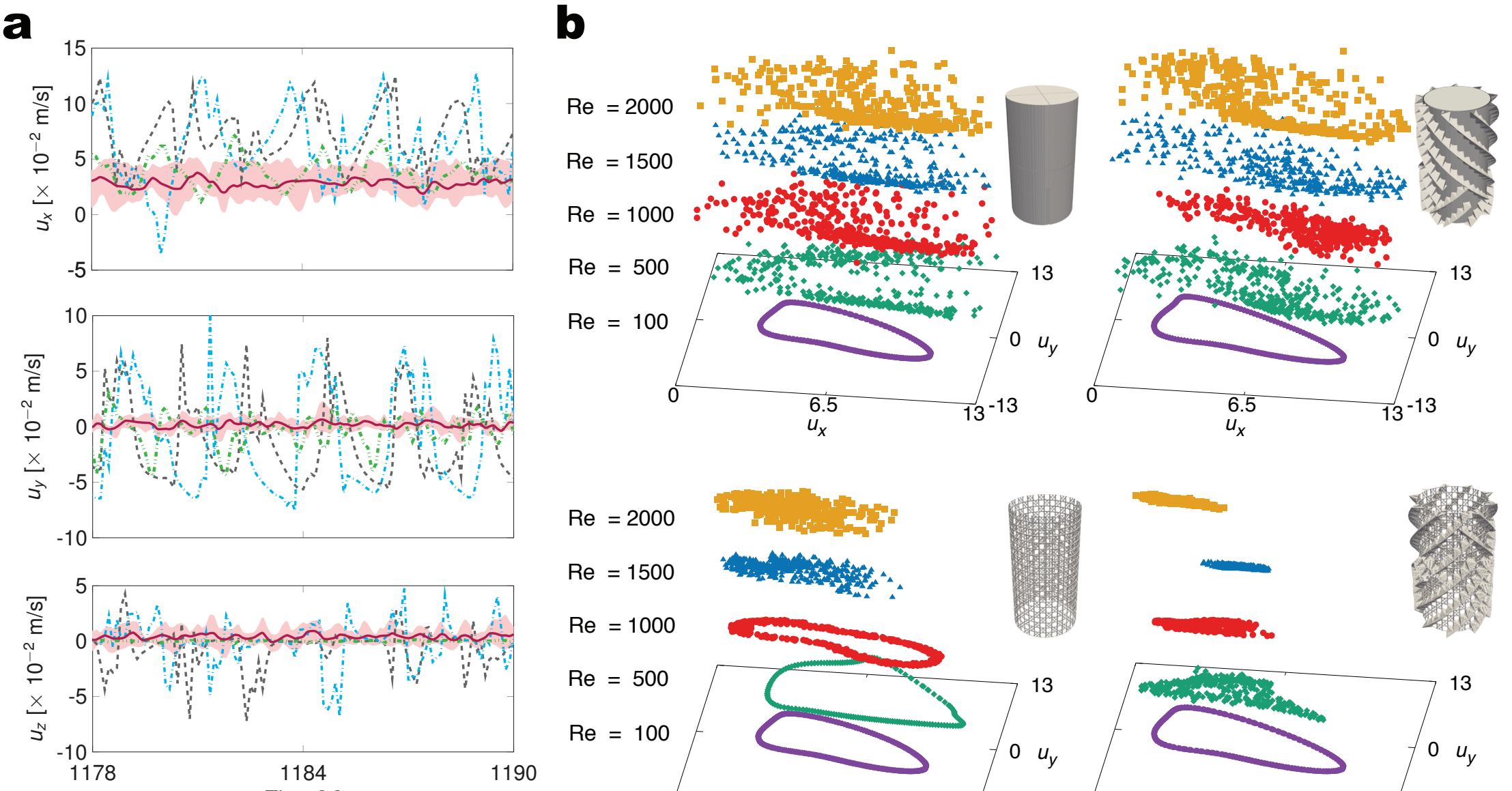
a
b
u_x [× 10^{-2} m/s]
u_y [× 10^{-2} m/s]
u_z [× 10^{-2} m/s]
15
10
5
0
-5
-10
1178
1184
1190
Re = 2000
Re = 1500
Re = 1000
Re = 500
Re = 100
0
6.5
13
u_x
u_y
-13

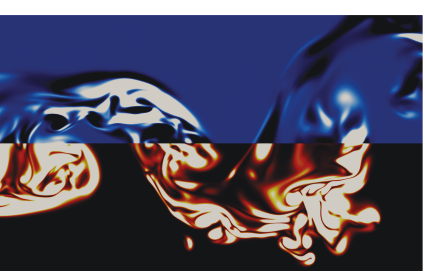

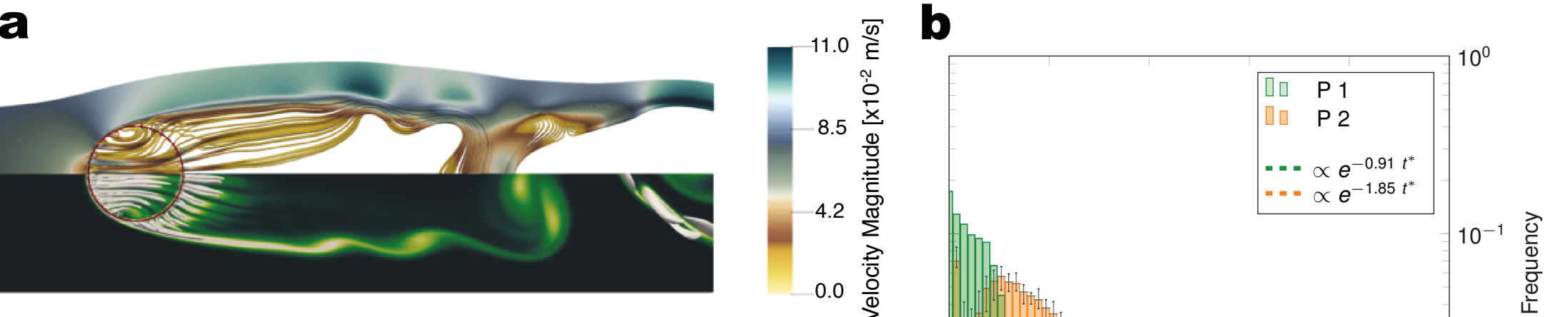
a
11.0
8.5
4.2
0.0
Velocity Magnitude [x10-2 m/s]
b
P 1
P 2
∝ e−0.91 t*
∝ e−1.85 t*
10^0
10^−1
Frequency